RSC Advances

PAPER

View Article Online
View Journal | View Issue

Cite this: *RSC Adv.*, 2026, **16**, 14547

Marigold-flower-like MoS_2 nanosheet assemblies for enhanced alkaline hydrogen evolution

Rajvardhan K. Chougale,[a] Prashant D. Sanadi,[a] Sanket N. Yadav,[b] Srinivaas Masimukku,[cd] Guo-Ping Chang-Chien,[de] Babasaheb D. Bhosale*[f] and Ganesh S. Kamble *[a]

The development of efficient, cost-effective, and noble-metal-free electrocatalysts is critical for sustainable hydrogen production *via* water splitting. Herein, hierarchical MoS_2 nanosheets were synthesized through a facile hydrothermal method, producing a marigold flower-like morphology with abundant exposed edge sites. Structural and compositional analyses using XRD, Raman, XPS, SEM, and BET confirmed the formation of crystalline, layered, and mesoporous MoS_2. Electrochemical evaluation in 1.0 M KOH revealed excellent hydrogen evolution reaction (HER) activity, with a low overpotential of 180 mV at 10 mA cm^{-2}, a Tafel slope of 122.3 mV dec^{-1}, and reduced charge-transfer resistance, highlighting efficient electron transport. Chronoamperometric measurements demonstrated outstanding long-term stability over 10 h. The combination of tailored morphology, high surface area, and favorable electronic structure establishes hydrothermally synthesized MoS_2 as a promising and practical electrocatalyst for sustainable hydrogen generation.

Received 1st January 2026
Accepted 25th February 2026

DOI: 10.1039/d6ra00011h

rsc.li/rsc-advances

1 Introduction

The increasing depletion of fossil fuel reserves and the severe environmental consequences associated with their consumption have intensified global efforts toward the development of sustainable and carbon-neutral energy technologies.[1–7] Among various clean energy vectors, hydrogen has emerged as a highly promising fuel due to its exceptionally high gravimetric energy density and environmentally benign combustion, which produces only water as a byproduct. In this context, electrochemical and photoelectrochemical water splitting have attracted considerable attention as a green route for hydrogen production. The overall efficiency of this process, however, is largely limited by the sluggish kinetics of the hydrogen evolution reaction (HER), which necessitates the development of highly active, stable, and cost-effective electrocatalysts to replace noble metals such as Pt.[8–15] Transition metal-based catalysts, particularly earth-abundant nanostructured materials, have gained significant interest as viable alternatives for HER applications. Among them, transition metal dichalcogenides (TMDs) have emerged as a distinctive class of layered materials with tunable electronic structures and excellent catalytic properties.[14,16–18] Molybdenum disulfide (MoS_2), a prototypical TMD, has been extensively explored owing to its suitable hydrogen adsorption free energy, high chemical stability, and layered structure composed of S–Mo–S units held together by van der Waals interactions. Notably, the catalytic activity of MoS_2 is predominantly associated with its edge sites, while the basal planes are relatively inert. However, recent pioneering studies have demonstrated that the basal plane can also become highly active when defects, atomic vacancies, or heteroatom substitutions are introduced. The spontaneous oxygen substitution in single-layer MoS_2 under ambient conditions has been shown to activate basal-plane sites and significantly enhance catalytic performance. Furthermore, transition-metal chalcogenide monolayers have been identified as versatile platforms for single-atom catalysis, where isolated metal atoms anchored on the basal plane act as highly efficient catalytic centers. In addition, several studies have reported that transition-metal doping—such as Pd and Ni can effectively modulate the electronic structure, create defect-rich active sites, and improve hydrogen evolution reaction activity.[19–22] Apart from these, polymorph-engineered MoS_2 can effectively modulate the electronic structure, create defect-rich active sites, and improve hydrogen evolution reaction activity.[23] These findings highlight that both edge-site engineering and basal-plane

[a]*Department of Engineering Chemistry, Kolhapur Institute of Technology's College of Engineering (Empowered Autonomous), Kolhapur Affiliated to Shivaji University, Kolhapur 416234, India. E-mail: ganeshchemistry2010@gmail.com; kamble.ganesh@kitcoek.in*

[b]*School of Nanoscience and Technology, Shivaji University, Kolhapur 416004, India*

[c]*Center for Environment Toxin and Emerging-Contaminant Research, Cheng Shiu University, Kaohsiung 833301, Taiwan, Republic of China*

[d]*Institute of Environment Toxin and Emerging-Contaminant, Cheng Shiu University, Kaohsiung 833301, Taiwan, Republic of China*

[e]*Conservation and Research Center, Cheng Shiu University, Kaohsiung City 833301, Taiwan, Republic of China*

[f]*Department of Chemistry, Rajaram College, Kolhapur, 416004, India. E-mail: bdb.bhosale@gov.in*

activation through defect creation or heteroatom doping are crucial strategies for enhancing the intrinsic catalytic performance of MoS_2-based electrocatalysts. Consequently, rational design strategies such as nano-structuring, defect engineering, phase modulation, and exposure of active edge sites are critical for enhancing HER performance. These attributes position MoS_2 as a compelling candidate for next-generation, noble-metal-free HER electrocatalysts.[24–27] The synthesis method plays a pivotal role in tailoring the morphology, crystallinity, defect density, and exposed active sites of MoS_2-based catalysts. In this regard, the hydrothermal method stands out as a versatile, scalable, and environmentally benign approach for synthesizing nanostructured TMDs with controlled size and morphology.[28–33] Hydrothermal synthesis enables uniform nucleation and growth under mild reaction conditions, facilitating the formation of few-layered or defect-rich MoS_2 structures that are highly favorable for HER. Furthermore, this method allows facile incorporation of dopants, heterostructure formation, and phase engineering, which collectively enhance charge transfer kinetics and catalytic efficiency. Therefore, hydrothermally synthesized MoS_2-based materials represent a promising pathway toward the development of efficient, durable, and economically viable HER electrocatalysts for sustainable hydrogen production.[34–39]

Extensive efforts have been devoted to overcoming the intrinsic limitations of pristine MoS_2 for HER and advancing its performance toward practical application. State-of-the-art strategies include phase engineering from the semiconducting 2H phase to the metallic 1T or mixed 1T/2H phases, which significantly enhances electrical conductivity and accelerates charge transfer kinetics.[40] Defect engineering, such as sulfur vacancies and edge-rich architectures, has been demonstrated to modulate the hydrogen adsorption free energy (ΔG_H^*) toward thermoneutral values, thereby improving HER activity. In recent years, hierarchical nanoflower-type architectures of transition-metal dichalcogenides have attracted considerable attention because they provide efficient electrolyte accessibility, high surface area, and abundant exposed edge sites, all of which are advantageous for electrochemical water splitting and energy storage applicates. In particular, MoS_2 nanosheets assembled into three-dimensional flower-like structures have been widely explored through hydrothermal routes, where controlled nucleation and anisotropic growth of marigold-like MoS_2 architectures integrated with MOF-derived N-doped carbon have been reported as high-capacity anode materials for sodium-ion batteries.[41] The MoS_2/MOF architectures integrated with MOF demonstrating that hierarchical nanosheet assemblies can significantly enhance electrochemical stability and charge transport. Similarly, Re-doped MoS_2 flower-like microspheres has been synthesized by hydrothermal method in which dopant-assisted growth and defect generation improved catalytic activity for hydrogen evolution.[42] Flower-like heteronanosheet arrays such as CoS_2/MoS_2 have also been fabricated *via* solution-based methods, where the assembly of ultrathin nanosheets into three-dimensional architectures resulted in enhanced active-site exposure and improved durability in alkaline hydrogen evolution reactions.[43] Moreover, in recent reviews of MoS_2 electrocatalysts emphasize that morphology engineering—especially the formation of nanoflower or hierarchical nanosheet assemblies—plays a key role in improving the intrinsic activity by increasing edge density and facilitating charge/mass transport.[44]

Furthermore, heteroatom doping (*e.g.*, Co, Ni, Fe) and construction of MoS_2-based heterostructures with carbon materials, metal oxides, or other transition metal compounds have shown synergistic effects, leading to reduced overpotentials, smaller Tafel slopes, and enhanced durability across a wide pH range. These advancements have enabled MoS_2-based electrocatalysts to approach or, in some cases, rival the performance of noble-metal catalysts, positioning MoS_2 as a benchmark non-precious HER catalyst and a cornerstone material in next-generation hydrogen energy technologies.[45–49] Despite these advances, controlling the assembly of two-dimensional MoS_2 nanosheets into well-defined hierarchical flower-like architectures remains challenging, and subtle variations in precursor composition, reaction environment, and growth kinetics can significantly influence morphology and catalytic performance. Therefore, developing simple and reproducible synthesis strategies to obtain hierarchical MoS_2 nanosheet assemblies with enhanced electrochemical activity is still of considerable interest.

In this work, we report a marigold-like assembly of MoS_2 nanosheets synthesized *via* a controlled hydrothermal route to obtain nanostructures with enhanced exposure of active edge sites and catalytic performance toward alkaline hydrogen evolution. The material was comprehensively characterized using PXRD, Raman spectroscopy, XPS, and electron microscopy to confirm phase composition, defect chemistry, and morphology. Electrochemical studies revealed excellent HER performance, delivering a low overpotential at 10 mA cm^{-2}, a small Tafel slope, and good long-term stability, demonstrating the effectiveness of hydrothermal engineering in activating MoS_2 as an efficient noble-metal-free HER electrocatalyst.

2 Materials and methods

2.1 Materials

All chemicals used in the present investigation were of analytical reagent (AR) grade and were used without further purification. Sodium molybdate dihydrate ($Na_2MoO_4 \cdot 2H_2O$) and the sulfur (S) source were procured from Sigma-Aldrich. Absolute ethanol (99.5% purity, Sigma-Aldrich) was used as the solvent, while a 35% (w/w) aqueous solution of hydrochloric acid (HCl, Sigma-Aldrich) served as the catalyst. The pH of the reaction medium was adjusted using ammonium hydroxide (NH_4OH, Sigma-Aldrich). Double-distilled water (DDW) was used throughout for the preparation of all solutions.

2.2 Synthesis of MoS_2 *via* hydrothermal method

The MoS_2 nanoparticles were synthesized utilizing the hydrothermal method. A total of 0.4838 g (2 mmol) of sodium molybdate dihydrate ($Na_2MoO_4 \cdot 2H_2O$) was dissolved in DDW, to which 0.7612 g (10 mmol) of thiourea was added

incrementally with continuous stirring. The complete solution was then transferred into a 100 mL Teflon-lined stainless-steel autoclave and subjected to thermal treatment in an oven at 200 °C for 24 hours. Following this, the autoclave was allowed to cool to room temperature, and the solid nanoparticles of MoS_2 were subsequently washed with deionized water and anhydrous ethanol three times at 7000 rpm, respectively. The MoS_2 nanoparticles were then dried at 80 °C in a vacuum oven for 12 hours.

The controlled precursor ratio, gradual addition of thiourea, and extended reaction duration (200 °C, 24 h) play a crucial role in directing the nucleation and growth of two-dimensional MoS_2 nanosheets, which subsequently self-assemble into a three-dimensional hierarchical morphology. This subtle modification of reaction parameters results in improved nanosheet stacking, higher exposure of edge sites, and enhanced electrochemical activity.

The as-synthesized marigold-flower-like MoS_2 electrocatalyst differs from earlier studies[41–44] in several important aspects. For instance, previously reported marigold-flower-like MoS_2 structures often involve multi-step processes, dopant incorporation, required MOF templating and subsequent carbonization. Whereas, some of the marigold-like MoS_2 were fabricated through substrate-assisted growth to form heterostructured arrays rather than free-standing MoS_2 assemblies. In contrast, the present work employs a single-step hydrothermal route without dopants, and templates, enabling the direct self-assembly of ultrathin MoS_2 nanosheets into a marigold-like hierarchical architecture. The present approach represents a simplified and template-free route for obtaining marigold-like nanosheet assemblies with promising electrocatalytic performance.

2.3 Physico-chemical characterizations

X-ray diffraction (XRD) patterns were collected from a Rigaku D/Max-TTR III X-ray diffractometer with Cu Kα radiation (λ = 1.5406 Å) over the 2θ range of 5–90°. The Raman spectra were measured on a Renishaw UK Sales Model Renish INVIA 0120-20 Raman spectrometer. The morphology of the material was observed by the FE-SEM using JSM-6701F (JEOL, Japan). The Brunauer–Emmett–Teller (BET) instrument is a surface area analyzer that measures the surface area and porosity of a material the Anton Paar makes the NOVA 1000e model was used instrument. The XPS instrument used for surface area measurements was performed JEOL Japan Make, Model JPS-9030. X-ray photoelectron spectroscopy, which is a compositional characterization technique used at the Institution: Common Facility Centre (CFC)-Sophisticated Analytical Instrument Facilities (SAIF), Kolhapur.

2.4 Electrochemical measurements

Electrochemical measurements were carried out using a CH Instruments CHI 660 electrochemical workstation. A conventional three-electrode configuration was employed for the HER setup in 1.0 M KOH electrolyte (N_2-saturated, 30 mL electrochemical cell). Nickel foam (1 × 1 cm^2) served as the working electrode and was coated with catalyst ink prepared by ultrasonically dispersing 20 mg of ZCF-x in a mixed solvent containing 796 μL of deionized water, 200 μL of isopropyl alcohol, and 4 μL of Nafion solution. An Ag/AgCl electrode (3 M KCl) and a graphite rod were used as the reference and counter electrodes, respectively. Linear sweep voltammetry (LSV) was conducted to evaluate electrocatalytic activity, with all measured potentials converted to the reversible hydrogen electrode (RHE) scale using the Nernst equation.[50] Tafel plots were derived from the polarization curves to elucidate reaction kinetics.[51] Electrochemical impedance spectroscopy (EIS) measurements were performed with an AC perturbation of 5 mV over a frequency range of 1000 kHz to 0.1 Hz. Long-term electrocatalytic stability was assessed by chronoamperometry at a constant current density of 10 mA cm^{-2}, ensuring a comprehensive evaluation of catalytic activity, charge-transfer behavior, and durability.

3 Result and discussion

Fig. 1a presents the XRD pattern of the synthesized MoS_2 sample. The diffraction profile exhibits well-defined and sharp peaks, confirming the crystalline nature of the prepared material. The observed reflections at 2θ values of approximately 14.40°, 33.00°, 36.15°, 43.18°, and 58.23° can be indexed to the

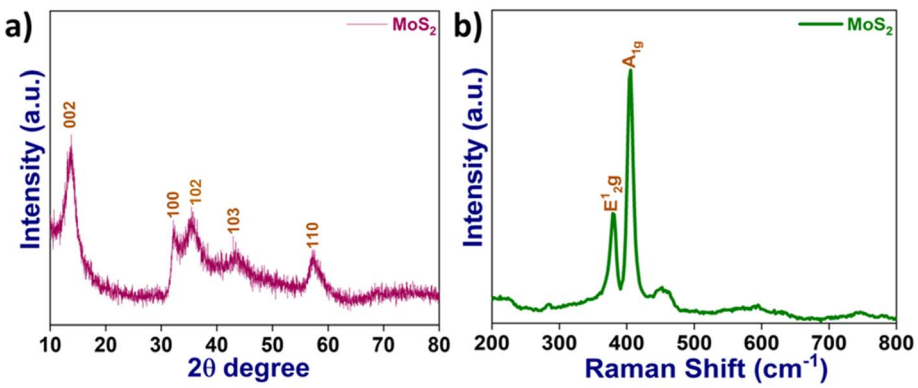

Fig. 1 (a) XRD pattern and (b) Raman spectrum of MoS_2, confirming its crystalline phase and characteristic vibrational modes.

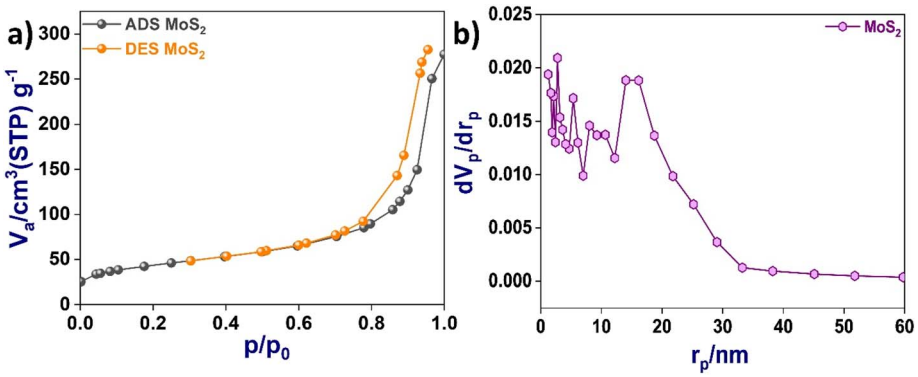

Fig. 2 (a) N_2 adsorption–desorption isotherms and (b) BJH pore size distribution of MoS_2, revealing its surface area characteristics and mesoporous nature.

(002), (100), (102), (103), and (110) crystallographic planes, respectively, in good agreement with the standard hexagonal phase of MoS_2 (JCPDS reference code no. 00-037-1492). The presence of the prominent low-angle (002) reflection indicates a layered structure with preferential orientation along the *c*-axis, characteristic of two-dimensional MoS_2 nanosheets. Such a well-defined lamellar architecture is highly desirable, as it promotes the exposure of catalytically active edge sites and facilitates charge transport, thereby rendering the synthesized MoS_2 particularly suitable for hydrogen evolution reactions.[52]

The Raman spectrum of the synthesized MoS_2 (Fig. 1b) exhibits two characteristic vibrational modes at 380 cm^{-1} and 405 cm^{-1}, corresponding to the in-plane E^1_{2g} and out-of-plane A^1_g phonon modes, respectively. These Raman features are the fingerprint of hexagonal 2H-MoS_2, confirming the successful formation of layered MoS_2 nanosheets.[53] The frequency separation ($\Delta \approx 24.9$ cm^{-1}) between the E^1_{2g} and A^1_g modes indicates the presence of few-layer MoS_2, which is known to enhance the exposure of active edge sites and improve charge transfer kinetics. Such structural characteristics are highly favorable for hydrogen evolution reaction (HER) applications.

The textural properties of the synthesized MoS_2 were evaluated using N_2 adsorption–desorption measurements (Fig. 2a and b). The Brunauer–Emmett–Teller (BET) analysis revealed a specific surface area of 18.45 m^2 g^{-1}, indicating the presence of accessible active sites for electrocatalytic reactions. The Barrett–Joyner–Halenda (BJH) pore size distribution showed an average pore radius of 2.89 nm, confirming the mesoporous nature of the material. The total pore volume was calculated to be 2.67 × 10^{-2} cm^3 g^{-1} for pores with radii below 78.27 nm, determined at a relative pressure (P/P_0) of 0.9876. This mesoporous architecture facilitates efficient electrolyte penetration and mass transport, which is advantageous for enhancing charge transfer and catalytic activity during the hydrogen evolution reaction.

The SEM images demonstrate that the as-synthesized MoS_2 exhibits a hierarchical marigold-like nanoflower morphology composed of interconnected and vertically aligned nanosheets (Fig. 3a and b), formed by the self-assembly of thin, crumpled nanosheets into three-dimensional hierarchical structures. Such three-dimensional assemblies of ultrathin MoS_2 sheets are consistent with previously reported flower-like MoS_2 architectures prepared *via* hydrothermal, solvothermal methods.[41–44] Earlier studies have shown similar hierarchical morphologies in doped or composite systems, where nanosheet assembly leads to increased surface area and exposure of catalytically active sites. However, unlike those systems, which often require dopants, templates, substrates, or multi-step synthesis, the

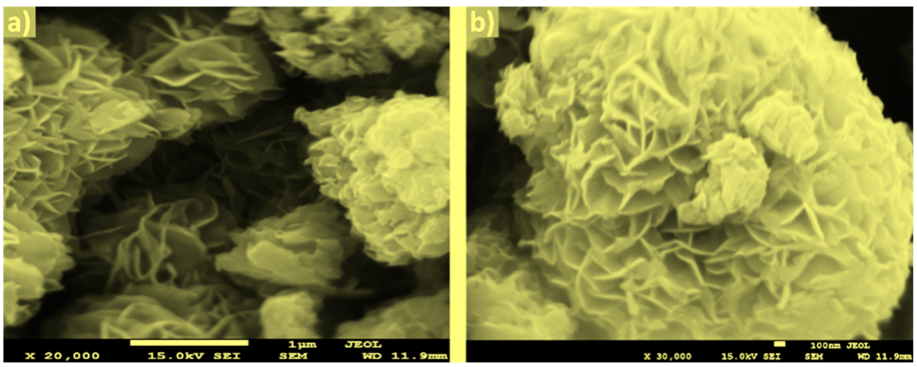

Fig. 3 (a and b) FE-SEM images of MoS_2 showing a well-defined flower-like morphology formed by the assembly of thin nanosheets, providing abundant exposed edges and active sites.

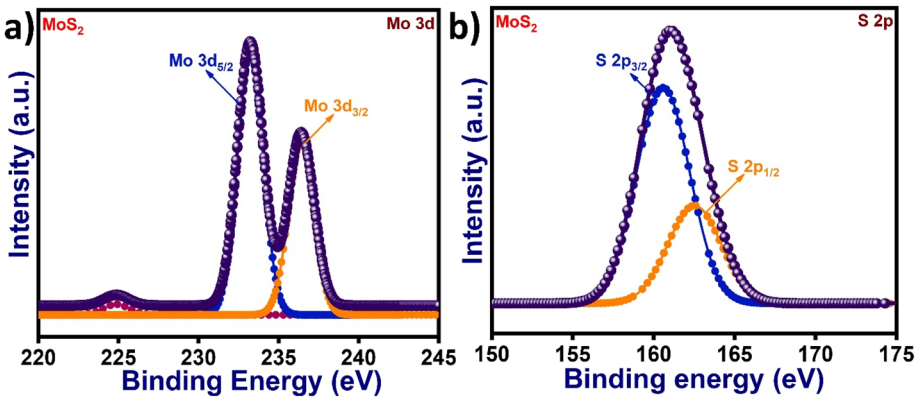

Fig. 4 Deconvoluted XPS spectra of MoS_2 showing (a) Mo 3d and (b) S 2p core levels, confirming the chemical states of Mo^{4+} and S^{2-} and the formation of stoichiometric MoS_2.

present material forms a free-standing marigold-like assembly through a single-step, template-free hydrothermal route. The nanosheets in the current structure appear relatively thin, loosely stacked, and hence significantly increases the surface roughness and exposes a large number of catalytically active edge sites, which may facilitate electrolyte penetration and augment the accessibility of edge and defect sites. This structural configuration is highly advantageous is comparable to earlier reports, thus charge transport and reaction kinetics has been improved resulted enhanced HER activity.

The deconvoluted XPS spectra of the synthesized MoS_2 provide insight into the chemical composition and electronic states of the material. The Mo 3d spectrum exhibits two prominent peaks at 233.00 eV and 236.44 eV, corresponding to Mo $3d_{5/2}$ and Mo $3d_{3/2}$, which are characteristic of Mo^{4+} in the MoS_2 lattice (Fig. 4a).[54] This confirms the successful incorporation of molybdenum in its expected oxidation state. The S 2p spectrum displays two peaks at 160.51 eV and 162.57 eV, assigned to S $2p_{3/2}$ and S $2p_{1/2}$, respectively, verifying the presence of sulfide species in the lattice (Fig. 4b).[55] Collectively, the XPS results confirm the stoichiometric formation of MoS_2 and support the structural integrity inferred from XRD, Raman, and electron microscopy analyses. These features are crucial for exposing active sites and enhancing electrocatalytic performance in the HER.

The HER activity of the MoS_2 catalyst was evaluated in 1.0 M KOH electrolyte using linear sweep voltammetry (LSV) at a scan rate of 10 mV s^{-1} (Fig. 5a). The presented LSV curves are with *iR*-correction and that all samples were measured under identical conditions, ensuring that the comparative electrocatalytic trends remain valid. As shown in Fig. 5a, the MoS_2-modified electrode exhibited a significantly lower overpotential of 142 mV at 10 mA cm^{-2} compared to 409 mV for bare Ni foam, highlighting the enhanced catalytic activity of the MoS_2 nanosheets. The kinetics of the MoS_2 were shown by the Tafel slope as illustrated in Fig. 5b, the corresponding Tafel slope for MoS_2 was derived from *iR*-corrected polarization curves and it is a 101.89 mV dec^{-1}, markedly smaller than that of Ni foam (157.12 mV dec^{-1}) indicating more favorable HER kinetics. The hydrogen evolution reaction in alkaline media generally proceeds through a Volmer–Heyrovsky mechanism involving two elementary steps. The Volmer step corresponds to the electrochemical discharge of water and adsorption of hydrogen on the catalyst surface:

$$H_2O + M + e^- \rightarrow M\text{–}H_{ads} + OH^- \text{ (rate-limiting step)}$$

This step involves water dissociation and formation of adsorbed hydrogen intermediates at the active sites (M). Subsequently, hydrogen evolution occurs *via* the Heyrovsky step:

$$H_2O + M\text{–}H_{ads} + e^- \rightarrow H_2 + OH^-$$

which represents the electrochemical desorption of hydrogen. In this case, M stands for "working sites." Based on the obtained Tafel slope (122.3 mV dec^{-1}), the HER over the MoS_2 electrode is suggested to follow a Volmer–Heyrovsky pathway, where the Volmer step is likely the rate-determining step. The layered structure and high surface area of MoS_2 provide abundant active sites that facilitate water dissociation and hydrogen adsorption in alkaline electrolyte, thereby enhancing HER kinetics. The observed Tafel slope is consistent with this mechanism and indicates that the catalytic process is governed by hydrogen adsorption followed by rapid electrochemical desorption. Electrochemical impedance spectroscopy (EIS) was further employed to probe the charge-transfer behavior of the electrodes. Compared with the bare Ni foam electrode, the MoS_2-modified electrode displayed a lower charge-transfer resistance (R_{ct}) (Fig. 5c), suggesting improved electrical conductivity and more efficient electron transport at the electrode–electrolyte interface. These features collectively demonstrate that the hydrothermally synthesized MoS_2 possesses abundant active sites, rapid charge transfer, and excellent electrocatalytic efficiency for HER in alkaline media. The long-term durability of MoS_2 was evaluated through a chronoamperometric *i–t* measurement at a constant current density in 1.0 M KOH for 48 hours (Fig. 5d). The catalyst exhibited negligible loss in current over the testing period, indicating excellent electrochemical stability and robust structural

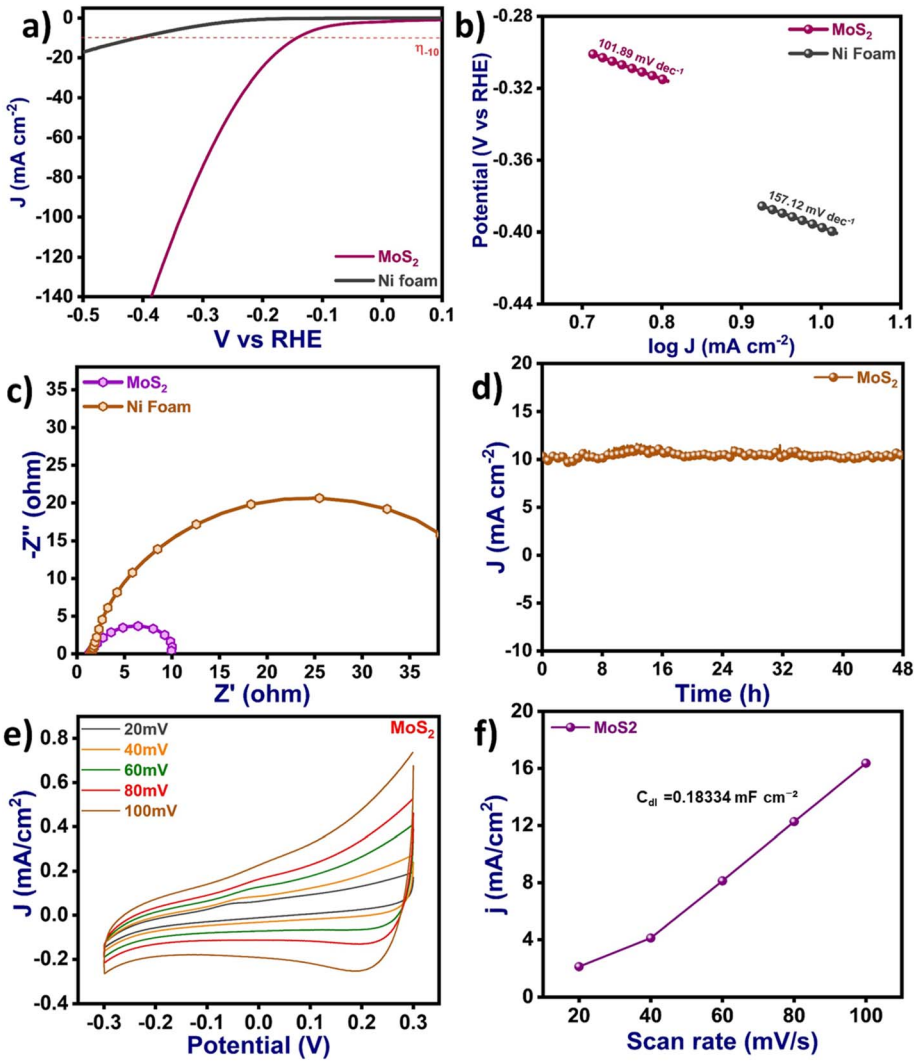

Fig. 5 Hydrogen evolution reaction (HER) performance of MoS_2 in alkaline electrolyte: (a) linear sweep voltammetry (LSV) polarization curves, (b) corresponding Tafel slope, (c) electrochemical impedance spectroscopy (EIS) Nyquist plot, and (d) long-term stability evaluated by chronoamperometry, demonstrating efficient activity and durable electrocatalytic performance, (e) CV measured at scan rates between 20 to 100 mV s^{-1}, (f) plot of current density at 0.2 V *vs.* RHE against scan rate for double layer capacitance calculation.

integrity under prolonged HER conditions. However, the long-term stability test was carried out at a current density of 10 mA cm^{-2}, which is widely used as a benchmark current density for evaluating electrocatalytic performance in water splitting at lab-scale and allows reliable comparison with previously reported catalysts in the literature.[22] The electrochemically active surface area (ECSA) of MoS_2 was evaluated from the double-layer capacitance (C_{dl}) obtained by cyclic voltammetry in the non-faradaic region at different scan rates (Fig. 5e). Based on the CV curve, the graph of current density at 0.2 V *vs.* RHE against scan rate as shown in Fig. 5f. The slope value is 0.18334 mF cm^{-2}, exhibited that MoS_2 electrode has elatively large electrochemically accessible surfaces. Using a standard specific capacitance (C_s) value of 40 μF cm^{-2} for metal sulfide-based electrodes, the corresponding ECSA was calculated to be approximately 4.58 cm^2. This enhanced ECSA suggests the presence of abundant exposed active sites, which can be attributed to the layered structure of MoS_2 with edge-rich domains and defect-induced surface roughness. The increased electrochemical surface area facilitates improved electrolyte–electrode interaction and faster charge transfer, thereby contributing to the favourable electrocatalytic performance of MoS_2.

4 Conclusion

In summary, hierarchical MoS_2 nanosheets were successfully synthesized *via* a facile hydrothermal method, yielding a well-defined marigold-flower-like morphology with abundant exposed edge sites. Comprehensive characterization using XRD, Raman, XPS, SEM, and BET analyses confirmed the crystalline nature, layered structure, chemical composition, and mesoporous architecture of the material. The MoS_2 catalyst exhibited excellent electrocatalytic activity for the HER in 1.0 M KOH,

achieving a low overpotential of 142 mV at 10 mA cm^{-2} and Tafel slope 101.89 mV dec^{-1}, and superior charge-transfer characteristics as revealed by EIS. Moreover, chronoamperometric testing demonstrated remarkable long-term stability over 48 h. These results highlight that hydrothermally engineered MoS_2 with optimized morphology and surface properties is a promising, cost-effective, and noble-metal-free electrocatalyst for sustainable hydrogen production.

Author contributions

Rajvardhan K. Chougale; methodology, writing – original draft. Prashant D. Sanadi; revision and writing – original draft. Sanket N. Yadav; validation, resources. Babasaheb D. Bhosale; supervision. Srinivaas Masimukku; resources, Guo-Ping Chang-Chien; resources, Ganesh S. Kamble; supervision, project administration, validation, investigation, conceptualization.

Conflicts of interest

There are no conflicts to declare.

Data availability

All raw data supporting BET, UV/Vis, Ramen and XRD is contained within the supplementary information (SI). Supplementary information is available. See DOI: https://doi.org/10.1039/d6ra00011h.

Acknowledgements

The authors (RKC, GSK) would want to express gratitude to the CFC-SAIF-DST Center, Shivaji University Kolhapur for the instrumentation facilities. The authors (RKC, GSK) have thankful to Chhatrapati Shahu Maharaj Research, Training and Human Development Institute (SARTHI), Pune (Government of Maharashtra) for the financial support.

References

1 W. Shang, Q. Li, X. Li, K. Zhang, B. Wang, Y. Lou and J. Chen, *Dalton Trans.*, 2023, **52**, 8613–8619.
2 H. Kamaruddin, Z. Jianghong, L. Yu, W. Yuefan and H. Yizhong, *J. Mater. Chem. A*, 2024, **12**, 9933–9961.
3 P. Dhiman and A. Kumar, *ACS Symp. Ser.*, 2025, **1474**, 73–98.
4 S. Wang, J. Wu, Y. Xu, D. Liang, D. Li, D. Chen, G. Liu and Y. Feng, *Small*, 2024, **20**, 2311221.
5 S. Xie, F. Li, S. Xu, J. Li and W. Zeng, *Chin. J. Catal.*, 2019, **40**, 1205–1211.
6 T. Song, X. Cai and Y. Zhu, *Nanoscale*, 2024, **16**, 13834–13846.
7 Y. Tao, M. Wu, M. Hu, X. Xu, M. I. Abdullah, J. Shao and H. Wang, *SusMat*, 2024, **4**, e230.
8 L. Fei, H. Sun, Y. Li, Y. Gu, W. Zhou and Z. Shao, *Energy Environ. Sci.*, 2025, **18**, 6456–6529.
9 L. Tang, X. Meng, D. Deng and X. Bao, *Adv. Mater.*, 2019, **31**, 1901996.
10 A. Mukherjee, N. Ojha, K. K. Pant, A. Deb, M. Abdinejad, S. S. Mahapatra and B. C. Ruidas, *Environ. Sci. Technol. Lett.*, 2025, **12**(9), 1113–1138.
11 S. Liu, Y. Shuli, C. Lin, Y. Hongjie, D. Kai, W. Ziqiang, X. You, W. Liang and H. Wang, *Energy Lab*, 2023, **1**, DOI: 10.54227/elab.20220005.
12 L. Zhang, W. Li, S. Ren, W. Song, C. Wang and X. Lu, *Adv. Energy Mater.*, 2025, **15**, 2403136.
13 P. Li, Q. Yang, H. Wu, J. Shang, F. Yan, X. Tong, T. Gan and L. Wang, *Energy Fuels*, 2025, **39**(14), 7047–7056.
14 Y. Shi, X. Feng, H. Guan, J. Zhang and Z. Hu, *Int. J. Hydrogen Energy*, 2021, **46**, 8557–8566.
15 O. Van Der Heijden, S. Park, R. E. Vos, J. J. J. Eggebeen and M. T. M. Koper, *ACS Energy Lett.*, 2024, **9**, 1871–1879.
16 K. Nguyen-Ba, J. R. Vargas-García and A. Manzo-Robledo, *Mater. Sci. Eng., B*, 2020, **256**, 114539.
17 A. Farooq, S. Khalil, B. Basha, A. Habib, M. S. Al-Buriahi, M. F. Warsi, S. Yousaf and M. Shahid, *Int. J. Hydrogen Energy*, 2024, **51**, 1318–1332.
18 W. Septina, C. P. Muzzillo, C. L. Perkins, A. C. Giovanelli, T. West, K. K. Ohtaki, H. A. Ishii, J. P. Bradley, K. Zhu and N. Gaillard, *J. Mater. Chem. A*, 2021, **9**, 10419–10426.
19 J. Pető, T. Ollár, P. Vancsó, Z. I. Popov, G. Z. Magda, G. Dobrik, C. Hwang, P. B. Sorokin and L. Tapasztó, *Nat. Chem*, 2018, **10**, 1246–1251.
20 P. Vancsó, Z. I. Popov, J. Pető, T. Ollár, G. Dobrik, J. S. Pap, C. Hwang, P. B. Sorokin and L. Tapasztó, *ACS Energy Lett.*, 2019, **4**, 1947–1953.
21 J. Gupta, D. Das, P. H. Borse and B. V. Sarada, *Sustainable Energy Fuels*, 2024, **8**, 1526–1539.
22 D. Wang, X. Zhang, Y. Shen and Z. Wu, *RSC Adv.*, 2016, **6**, 16656–16661.
23 H. Eidsvåg, P. Vajeeston and D. Velauthapillai, *ACS Omega*, 2023, **8**, 26263–26275.
24 S. Bolar, S. Shit, N. C. Murmu, P. Samanta and T. Kuila, *ACS Appl. Mater. Interfaces*, 2021, **13**, 765–780.
25 T. Tien and E. L. Chen, *Catalysts*, 2023, **13**(8), 1152.
26 B. S. Reghunath, S. Rajasekaran, S. Devi K R, D. Pinheiro and J. R. Jaleel UC, *Int. J. Hydrogen Energy*, 2023, **48**, 2906–2919.
27 J. Ni, Z. Shi, Y. Wang, J. Yang, H. Wu, P. Wang, M. Xiao, C. Liu and W. Xing, *eScience*, 2025, **5**, 100295.
28 M. Mulu, D. RamaDevi, N. Belachew and K. Basavaiah, *RSC Adv.*, 2021, **11**, 24536–24542.
29 F. Riyanti, W. Purwaningrum, N. Yuliasari, S. Putri, N. Aprianti and P. L. Hariani, *Turk. J. Chem.*, 2022, **46**, 1875–1882.
30 H. Yin, S. Su, D. Yao, L. Wang, X. Liu, T. T. Isimjan, X. Yang and D. Cai, *Inorg. Chem. Front.*, 2024, **11**, 2489–2497.
31 Z. Feng, P. Yang, G. Wen, H. Li, Y. Liu and X. Zhao, *Appl. Surf. Sci.*, 2020, **502**, 144129.
32 Y. Li, H. Wang, L. Xie, Y. Liang, G. Hong and H. Dai, *J. Am. Chem. Soc.*, 2011, **133**, 7296–7299.
33 D. E. Al Momani, F. Arshad, I. Taha, D. H. Anjum and L. Zou, *npj Clean Water*, 2024, **7**, 64.
34 A. Farooq, S. Khalil, B. Basha, A. Habib, M. S. Al-Buriahi, M. F. Warsi, S. Yousaf and M. Shahid, *Int. J. Hydrogen Energy*, 2024, **51**, 1318–1332.

35 T. Eisa, H. O. Mohamed, Y.-J. Choi, S.-G. Park, R. Ali, M. A. Abdelkareem, S.-E. Oh and K.-J. Chae, *Int. J. Hydrogen Energy*, 2020, **45**, 5948–5959.
36 N. Han, M. Race, W. Zhang, R. Marotta, C. Zhang, A. Bokhari and J. J. Klemeš, *J. Cleaner Prod.*, 2021, **318**, 128544.
37 J. Han, Q. Liu, Y. Yang and H. B. Wu, *Chem. Sci.*, 2025, **16**, 3788–3809.
38 P. D. Sanadi, R. K. Chougale, D. B. Malavekar, J. H. Kim, S. Masimukku, G.-P. Chang-Chien, Y.-C. Ling, S. S. Kolekar and G. S. Kamble, *Sci. Rep.*, 2025, **15**, 16074.
39 M. S. S. Danish, *RSC Sustainability*, 2023, **1**, 2180–2196.
40 Y. Jiang, S. Li, F. Zhang, W. Zheng, L. Zhao and Q. Feng, *Catal. Commun.*, 2021, **156**, 106325.
41 S. Priya, R. Ravindran, P. De, D. Mandal, S. Mahato, S. Kansal and A. Chandra, *ACS Appl. Energy Mater.*, 2024, **7**, 594–603.
42 J. Aliaga, P. Vera, J. Araya, L. Ballesteros, J. Urzúa, M. Farías, F. Paraguay-Delgado, G. Alonso-Núñez, G. González and E. Benavente, *Molecules*, 2019, **24**, 4631.
43 M. Shi, Y. Zhang, Y. Zhu, W. Wang, C. Wang, A. Yu, X. Pu and J. Zhai, *RSC Adv.*, 2020, **10**, 8973–8981.
44 T. Van Nguyen, M. Tekalgne, T. P. Nguyen, Q. Van Le, S. H. Ahn and S. Y. Kim, *Battery Energy*, 2023, **2**, 20220057.
45 W. Xu, Y. Tao, H. Zhang, J. Zhu, W. Shao, J. S. Sun, Y. Xia, Y. Ha, H. Yang, T. Cheng and X. Sun, *Small*, 2024, **20**(49), DOI: 10.1002/smll.202407328.
46 T. Lin, R. Xu, Y. Hu, J. Wang, Y. Liu and W. Zhou, *Int. J. Hydrogen Energy*, 2024, **68**, 688–695.
47 Z. Zheng, L. Yu, M. Gao, X. Chen, W. Zhou, C. Ma, L. Wu, J. Zhu, X. Meng, J. Hu, Y. Tu, S. Wu, J. Mao, Z. Tian and D. Deng, *Nat. Commun.*, 2020, **11**, 3315.
48 J. Wang, W. Fang, Y. Hu, Y. Zhang, J. Dang, Y. Wu, H. Zhao and Z. Li, *Catal. Sci. Technol.*, 2020, **10**, 154–163.
49 T. Manyepedza, J. M. Courtney, A. Snowden, C. R. Jones and N. V. Rees, *J. Phys. Chem. C*, 2022, **126**, 17942–17951.
50 M. Burud, V. Jadhav, A. Pattanshetti, P. Chougale, V. Chavan, H. Kim, S. A. Patil, D. Kim, A. Supale and S. Sabale, *New J. Chem.*, 2024, **48**, 18506–18513.
51 W. Y. Noh, S. J. Kazmouz, S. H. Lee, J. K. Peng, T. J. Shin and M. Shviro, *Energy Environ. Sci*, 2025, **18**, 8679–8696.
52 H. Gupta, S. Chakrabarti, S. Mothkuri, B. Padya, T. N. Rao and P. K. Jain, *Mater. Today: Proc.*, 2020, **26**, 20–24.
53 R. Luo, W. W. Xu, Y. Zhang, Z. Wang, X. Wang, Y. Gao, P. Liu and M. Chen, *Nat. Commun.*, 2020, **11**, 1011.
54 B. Li, L. Jiang, X. Li, P. Ran, P. Zuo, A. Wang, L. Qu, Y. Zhao, Z. Cheng and Y. Lu, *Sci. Rep.*, 2017, **7**, 11182.
55 M. Sojková, P. Siffalovic, O. Babchenko, G. Vanko, E. Dobročka, J. Hagara, N. Mrkyvkova, E. Majková, T. Ižák, A. Kromka and M. Hulman, *Sci. Rep.*, 2019, **9**, 2001.